INORGANIC CHEMISTRY
FRONTIERS

CHINESE CHEMICAL SOCIETY

ROYAL SOCIETY OF CHEMISTRY

RESEARCH ARTICLE

View Article Online
View Journal | View Issue

Check for updates

Cite this: *Inorg. Chem. Front.*, 2024, **11**, 2105

Hg_3AsS_4X (X = Cl and Br): two Hg-based chalcogenides as long-wave infrared nonlinear optical crystals with superior comprehensive performances†

Feng Xu,[a,c,d] Xiang Xu,[a,d] Bingxuan Li,[e] Ge Zhang,[e] Chan Zheng,*[a,c] Jindong Chen*[b] and Ning Ye*[b]

Received 4th January 2024,
Accepted 19th February 2024

DOI: 10.1039/d4qi00032c

rsc.li/frontiers-inorganic

Long-wave infrared (IR) nonlinear optical (NLO) crystals hold great promise for extensive applications. However, IR NLO crystals with outstanding comprehensive optical and NLO performances are still in great demand. Herein, two Hg-based chalcogenides, Hg_3AsS_4Cl and Hg_3AsS_4Br, are synthesized *via* a chemical vapor transport technique. Attributed to the synergistic combination of $[HgS_3]$ groups and structurally aligned $[AsS_3]$ groups with lone pair electrons, the two compounds exhibit superior NLO performance, encompassing strong second-harmonic generation (SHG) effects, tremendous birefringence, and a broad transparency range, positioning them as promising long-wave IR NLO materials. Moreover, the luminescent performances of the two compounds are also investigated, revealing interesting ultraviolet (UV) region luminescence emissions, broad emission bands, and large Stokes shifts for potential luminescent applications.

Introduction

Long-wave infrared (IR) lasers, which generate mid-infrared (MIR) (2.5–25 μm) coherent light through the frequency conversion process of nonlinear optical (NLO) crystals, has shown important applications in photoelectric countermeasures, laser guidance, infrared remote sensing, atmospheric detection, *etc.*[1–5] As the core device of tunable IR lasers, IR NLO crystals are in urgent demand. In fact, the difficulties involved in exploring IR NLO crystals are primarily centred around achieving a balance between second-harmonic generation (SHG) effects, laser damage thresholds (LDT), birefringence and IR transparency.[6–8] However, these NLO properties are strongly interconnected and contradictory,[9,10] which presents a huge challenge. For instance, large SHG coefficients of $ZnGeP_2$ crystal render it an excellent IR NLO crystal. However, the small band gap and multi-photon absorption of $ZnGeP_2$ in the 1064 nm hinder its serviceable range and further applications.[11] In view of this, for extensive applications, it is indispensable to screen novel long wave IR NLO crystals with superior performance covering sufficient phase-matching (PM) SHG intensity, a wide IR transmission range, moderate band gap and large birefringence.

Recently, d-block-metal-based chalcogenides have been proven to be a promising system for designing IR NLO crystals, especially Hg-based chalcogenides have attracted significant attention due to the unique electronic configuration of Hg.[12–14] Usually, highly polarized Hg^{2+} ions, stemming from the decreased shielding power of 4f electrons and relativistic effects, give rise to outstanding SHG effects and birefringence.[15,16] Hg atoms and chalcogen (Q) can also be aggregated into linear or V-shaped $[HgQ_2]^{2-}$, π-conjugated planar triangle $[HgQ_3]^{4-}$, tetrahedral $[HgQ_4]^{6-}$ and so on, which are beneficial for enriching the Hg-based chalcogenides structures.[17,18] Moreover, Hg atoms with a d^{10} electronic configuration can effectively avoid harmful d–d electronic transitions,[19] and form desired triangular and tetrahedral coordination modes.[20] Furthermore, as a heavy-metal element, Hg facilitates relatively wide IR transmission regions.[21,22] Lately, many promising favorable Hg-based chalcogenides IR NLO crystals were discovered, such as $Hg_3P_2S_8$ (4.2 × $AgGaS_2$

---

[a] *School of Materials Science and Engineering, Fujian University of Technology, Fuzhou 350118, China. E-mail: czheng.fjut@gmail.com*
[b] *Tianjin Key Laboratory of Functional Crystal Materials, Institute of Functional Crystal, Tianjin University of Technology, Tianjin 300384, China. E-mail: cjd1225@email.tjut.edu.cn, nye@email.tjut.edu.cn*
[c] *Institute of Biology and Chemistry, Fujian University of Technology, Fuzhou 350118, China*
[d] *State Key Laboratory of Structural Chemistry, Fujian Institute of Research on the Structure of Matter, Chinese Academy of Sciences, Fuzhou 350002, PR China*
[e] *Key Laboratory of Optoelectronic Materials Chemistry and Physics, Fujian Institute of Research on the Structure of Matter, Chinese Academy of Sciences, Fuzhou, Fujian 350002, China*

† Electronic supplementary information (ESI) available: Crystallographic data, measurements of physical properties, and theoretical calculations. CCDC 2311783 and 2311784. For ESI and crystallographic data in CIF or other electronic format see DOI: https://doi.org/10.1039/d4qi00032c

(AGS)),[23,24] $HgCuPS_4$ (6.5 × AGS),[19] $AHgSnS_4$ (A = Sr, Ba) (2.8/1.9 × AGS),[25] $Na_2Hg_3M_2S_8$ (M = Si/Ge/Sn) (1.3/2.2/2.8 × AGS),[26] $AHgPS_4$ (A = Na/K) (∼3.14/4.15 × AGS),[27] $[Ba_4Cl_2][HgGa_4S_{10}]$ (1.5 × AGS),[28] $AXHg_3P_2S_8$ (A = Rb, Cs; X = Cl, Br) (∼1 × AGS),[29] and so on. Inspired by the previous work mentioned above, we attempted to seek out Hg-based chalcogenides with favorable overall properties as potential IR NLO crystals. To improve NLO performance, metals (M = As, Sb, Sn and Te) with lone pair electrons, promoting preferable NLO effects,[30–35] were introduced to form trigonal pyramids as promising building units, facilitating synergetic tuning with Hg-based groups to balance the SHG effect, band gap, and birefringence comprehensively. Following the introduction of the above building units, the directivity of groups can also be adjusted and perfected for improved NLO performance according to the anionic group theory.[36] In addition, since halogen ions possess strong electronegativity, they can be taken into consideration for effectively enlarging the band gap.[37] As a result, two Hg-based chalcogenides, Hg_3AsS_4X (X = Cl and Br) (HASC and HASB), with the above desired structure configuration were synthesized by the chemical vapor transport technique.[38,39] Furthermore, their linear optical and NLO properties, thermal behavior as well as first principle calculations were studied by combining experiments and calculations, exhibiting favorable comprehensive optical and NLO performances. Additionally, to further exploit their practical application value, the luminescent performance of HASC and HASB was also preliminarily characterized, respectively, both intriguingly showing an emission band centered in the ultraviolet (UV) region at room temperature even though they were semiconductors. This work further revealed the superiority of HASC and HASB for expansive optical and NLO applications.

Experimental

Polycrystalline synthesis

All of the chemicals, HgS (Adamas, 3N), S (Taitan, 4N), As (Aladdin, 4N), $HgCl_2$ (Taitan, 3N), and $HgBr_2$ (Adamas, 3N) were purchased and used without further purification. Single crystals of HASC and HASB were synthesized by a chemical vapor transport method utilizing HgS, S, As, and $HgCl_2$/$HgBr_2$ at the molar ratios of 5 : 3 : 2 : 1 as raw materials, respectively. A mixture of the materials was placed in a silica tube with an inner diameter of 12 mm and a length of 150 mm, then flame-sealed under vacuum, and lain in a horizontal muffle furnace equipped with dual temperature zones, where the vaporization zone was heated at 400 °C while the crystallization zone was heated at 340 °C for 3 days. Then the silica tubes were decreased to room temperature at a rate of 5 °C h^{-1}. The polycrystalline HASC and HASB were obtained in the crystallization zone. The HASC and HASB crystals were all nonhygroscopic and stable in the air for months without showing oxidation or degradation. **Caution:** HgS, As, $HgCl_2$, and $HgBr_2$ are toxic, handling of these reagent requires a lot of precautions to avoid any skin contact and inhalation, and all operations should be carried out in an Ar-protected glovebox or fume cupboard.

Single crystal structure characterization

The crystal structure was determined by single-crystal X-ray diffraction. Single crystal X-ray diffraction data were collected at room temperature on a XtaLAB Synergy R diffractometer with Mo K_α radiation (λ = 0.71073 Å) using the ω-scan mode. The data was reduced and integrated with the CrysAlisPro program, and the absorption correction was achieved by the Multiscan technique. The single crystal structures were characterized by direct methods with full-matrix least-squares fitted on F^2 with SHELXL.[40,41] All the atoms were determined with anisotropic displacement parameters. The validity of structures were certified on the ADDSYM algorithm from PLATON program,[42] simultaneously, no higher symmetries were found.

Powder X-ray diffraction (PXRD)

The PXRD analysis of polycrystalline materials was achieved on a Miniflex-600 diffractometer using Cu K_α radiation (λ = 1.540598 Å) at room temperature with an angular scanning range of 2θ = 5°–85°, a scan step width of 0.02° and a scan speed of 0.2° min^{-1}.

Energy dispersive X-ray spectroscope (EDS) analysis

The EDS analysis was carried out on a field emission scanning electron microscope (FESEM, SU-8010) equipped with an energy dispersive X-ray spectrometer. The cleaned crystals were placed on an aluminum sample stage with carbon conductive tape. Different regions on the crystals were tested.

UV-Vis-NIR transmittance spectroscopy

The UV-Vis-NIR transmittance data of single crystals were recorded by utilizing polished crystal wafers at room temperature from 300 to 2500 nm on a PerkinElmer Lamda-950 UV-Vis-NIR spectrophotometer. The indirect band gap value was obtained by plotting absorption spectra with a Tauc function.

Fourier-transform infrared (FT-IR) spectroscopy

IR spectra of materials were performed on a Bruker VERTEX 70 FT-IR spectrometer with the help of polished crystal wafers in the range of 4000–400 cm^{-1}.

Raman spectrum measurement

The Raman spectrum in the range of 4000–50 cm^{-1} was measured on Horiba Labram HR800 evolution Raman spectrometer under a laser excitation at 633 nm.

Single crystal laser damage threshold (LDT) measurements

The LDT of single crystals was performed utilizing polished crystal wafers by a single pulse method. A power-tunable 1064 nm laser with a pulse width τ_p of 10 ns and an operating frequency of 1 Hz was employed to radiate the single crystal surface with a beam spot diameter of 1.3 mm. The input laser intensities were raised from 5 mJ until a fixed size damage spot occurs and the laser energy E was recorded. The LDT value was calculated from the equation $I(\text{threshold}) = E/(\pi r^2 t)$. To ensure reliability, the LDT value was obtained from the mean value of five measured samples.

Thermal analysis

The TG and DTA analysis were tested on a NETZSCH STA449F3 simultaneous analyzer under N_2 atmosphere. Reference (Al_2O_3 crucible) and polycrystalline samples (10 mg) packed in the same Al_2O_3 crucible were heated from 30 to 600 °C at a rate of 10 °C min^{-1} simultaneously and then cooled to room temperature naturally.

SHG measurements

Polycrystalline SHG signals were measured according to a modified Kurtz and Perry method using 2.05 μm laser radiation.[43] Since SHG efficiencies are known to depend strongly on particle size, polycrystalline samples of good quality were ground and sieved into the following particle size ranges: 25–45, 45–62, 62–75, 75–109, 109–150, and 150–212 μm. As a reference, the polycrystalline AGS was also ground and sieved into the same particle size ranges. The samples in different particle sizes were pressed between two glass microscope cover slides with a thickness of 1 mm and equipped with a 2 mm thick rubber ring, containing an 8 mm diameter hole in the center, which were tightly sheathed in aluminous holders with a central hole the same size as the rubber ring. The samples were then placed in a light-tight box and under the irradiation of a pulsed laser. In the process of the measurements, the background flash-lamp light on the sample can be limited by a cutoff filter, while the second harmonic signals can be selected by an interference filter and detected with a photomultiplier tube attached to a RIGOL DS1052E 50 MHz oscilloscope. Finally, the ratio of the second-harmonic intensity outputs between the samples and reference can be calculated clearly.

Luminescent measurements

The photoluminescence (PL) excitation spectra and emission spectra were recorded on an FLS980 spectrometer (Edinburgh) equipped with a continuous xenon lamp (450 W). The measurements were carried out in the range of 230–600 nm at room temperature. PL decay curves were measured with the FLS980 spectrometer equipped with a tunable optical parametric oscillator (OPO) pulse laser as the excitation source (225–2200 nm, Carlsbad, CA, USA). The power-dependent PL intensity was also performed in the FLS980 spectrometer by using an OPO pulse laser source and a Glan prism for power regulation. The low temperature measurements were carried out to cover the temperature of 10–300 K by mounting samples on a closed cycle cryostat (CS202PE-DMX-1AL, 10–300 K).

Computational details

Electronic structures, optical properties, and the DOS of HASC and HASB were analyzed by first-principles calculations based on the DFT calculation, utilizing the plane wave pseudopotential method with CASTEP code.[44,45] Generally, the exchange and correlative potential of electron–electron interactions were represented by generalized gradient approximation (GGA) in the scheme of Perdew–Burke–Ernzerhof (PBE).[46] Furthermore, the effective interaction between atom cores and valence electrons of each element was described through the norm-conserving pseudopotentials in the Kleinman–Bylander form,[47] where the valence electrons were expressed as Hg $5d^{10}6s^2$, As $4s^24p^3$, S $2s^22p^2$, Cl $3s^23p^5$, and Br $4s^24p^5$ electrons. Besides, the *k*-point of the first Brillouin zone of HASC and HASB was sampled as the 2 × 2 × 2 and 2 × 2 × 2 Monkhorst–Pack scheme,[48] respectively, which was used to calculate the optical properties and DOS of the crystal. During the calculation of the optical properties for HASC and HASB, the energy cutoff was set to be 600 eV and 400 eV, while self-consistent convergence of the total energy was set to be 2.0×10^{-6} eV per atom, respectively. In addition, the scissors operation was adopted in the dielectric function calculation owing to the underestimation of the band gap of the DFT method,[49] where a scissors operator of 0.921 eV and 0.822 eV for HASC and HASB, respectively, was applied to move the simulated band gap to the right place. The calculated SHG coefficients were calculated from the "velocity-gauge" formula,[50] while the SHG density was calculated by the band-resolved method.[51]

Results and discussion

PXRD and EDS analysis

The single crystals of HASC and HASB were obtained *via* a chemical vapor transport reaction (Fig. S1†). The PXRD patterns were identical to the simulated pattern from the single crystal models (Fig. S2†), confirming the purity of samples. The pure samples were used for subsequent characterizations. The EDS analysis further showed the presence of Hg/As/S/Cl/Br elements, respectively (Fig. S3†).

Crystal structure

The compounds, HASC and HASB, all crystallized in the NCS space group $P6_3mc$ of the hexagonal crystal system with unit cell parameters of $a = b = 7.4498(4)$ Å, $c = 9.0224(9)$ Å, $\alpha = \beta = 90°$, and $\gamma = 120°$, $Z = 2$ for HASC, $a = b = 7.4368(4)$ Å, $c = 9.3468(8)$ Å, $\alpha = \beta = 90°$, $\gamma = 120°$, and $Z = 2$ for HASB. Relevant crystallographic data and detailed structure refinement information are listed in Table 1. Besides, the data of the atomic coordinates, isotropic displacement parameters, bond lengths and angles, and anisotropic displacement parameters are shown in Tables S1–S3 in the ESI,† respectively. Since they were isostructural and crystallized in the same polar space group, the structure of HASC was analyzed as a representative sample and is shown in Fig. 1. There are 5 crystallographically independent sites including one Hg atom, one As atom, one Cl atom and two S atoms in one asymmetric unit. The basic structural unit was Hg-based $[Hg_3S_6]$ groups with 3-connected $[HgS_3]$ triangles (Fig. 1a), which was arranged regularly. The Hg–S bond distances of the $[Hg_3S_6]$ group varied from 2.449(3) to 2.519(2) Å, while the S–Hg–S and Hg–S–Hg bond angles were presented between 110.32(17)–123.60(6)° and 95.76(18)–

Table 1 Crystal data and structure refinement of HASC and HASB

Formula	Hg_3AsS_4Cl	Hg_3AsS_4Br
Formula mass (amu)	840.36	884.84
Temperature (K)	293(2)	293(2)
λ (Å)	0.71073	0.71073
Crystal system	Hexagonal	Hexagonal
Space group	$P6_3mc$	$P6_3mc$
a (Å)	7.4498(4)	7.4368(4)
b (Å)	7.4498(4)	7.4368(4)
c (Å)	9.0224(9)	9.3468(8)
α (°)	90	90
β (°)	90	90
γ (°)	120	120
V (Å^3)	433.65(6)	447.68(6)
Z	2	2
ρ (calcd) (g cm^{-3})	6.436	6.564
μ (mm^{-1})	57.939	60.288
F(000)	708	744
θ (°)	3.157–30.046	3.163–30.397
Index range	$-10 \le h \le 6$, $-7 \le k \le 9$, $-8 \le l \le 12$	$-10 \le h \le 9$, $-9 \le k \le 9$, $-9 \le l \le 13$
Reflections collected/unique	1715/396	1681/395
R_{int}	0.0265	0.0521
Completeness to θ = 25.242° (%)	100	100
GOF on F^2	0.993	1.075
R_1/wR_2 $[F_o^2 > 2\sigma(F_o^2)]^a$	0.0227/0.0484	0.0327/0.0714
R_1/wR_2 (all data)	0.0257/0.0490	0.0356/0.0722
Flack parameter	0.013(13)	0.02(2)

[a] $R_1(F) = \sum||F_o| - |F_c||/\sum|F_o|$, $wR_2(F_o^2) = [\sum w(F_o^2 - F_c^2)^2/\sum w(F_o^2)^2]^{1/2}$.

98.48(13)°, respectively. Besides, another structural unit, the $[AsS_3]$ trigonal pyramids, were introduced for improving NLO properties and structural directivity, where the As atom was coordinated to three S atoms (Fig. 1b). The As–S bond distance of $[AsS_3]$ group was 2.274(4) Å, while the S–As–S bond angles were 93.59(16)°. The $[Hg_3S_6]$ and $[AsS_3]$ groups were constructed by bridging S atoms, building a $[Hg_3AsS_4]^+$ layer (Fig. 1c). The layers alternately rotated 180°, which was attributed to the lone pair electron repulsion between the As atoms from neighbouring layers, generating an aligned arrangement of groups and strong polarity along the *c*-axis, inducing superior SHG effects and birefringence. The layers were arranged infinitely in the space through the Cl atoms, forming a distinct three-dimensional framework (Fig. 1d) and producing cavities surrounded by Cl^- as counter anions. The introduction of Cl^- ions was not only conducive to enlarging the band gap, but also reinforced interlayer interaction, where every Cl^- ion captured six near Hg^{2+} cations through strong electrostatic interactions from the adjacent layer (Fig. 1e), respectively, decreasing the interlayer spacing and creating favorable growth conditions.[9] It is worth noting that the $[Hg_3S_6]$ groups were slightly corrugated due to above electrostatic attraction of Cl^- ions toward Hg^{2+}, whereas all $[AsS_3]$ groups were uniformly arranged along the *c*-axis with a structure criterion (C) of 1 (present in Fig. 1d and section of computation), which means that the $[AsS_3]$ groups were optimally arranged, contributing to optimization of the NLO performance.

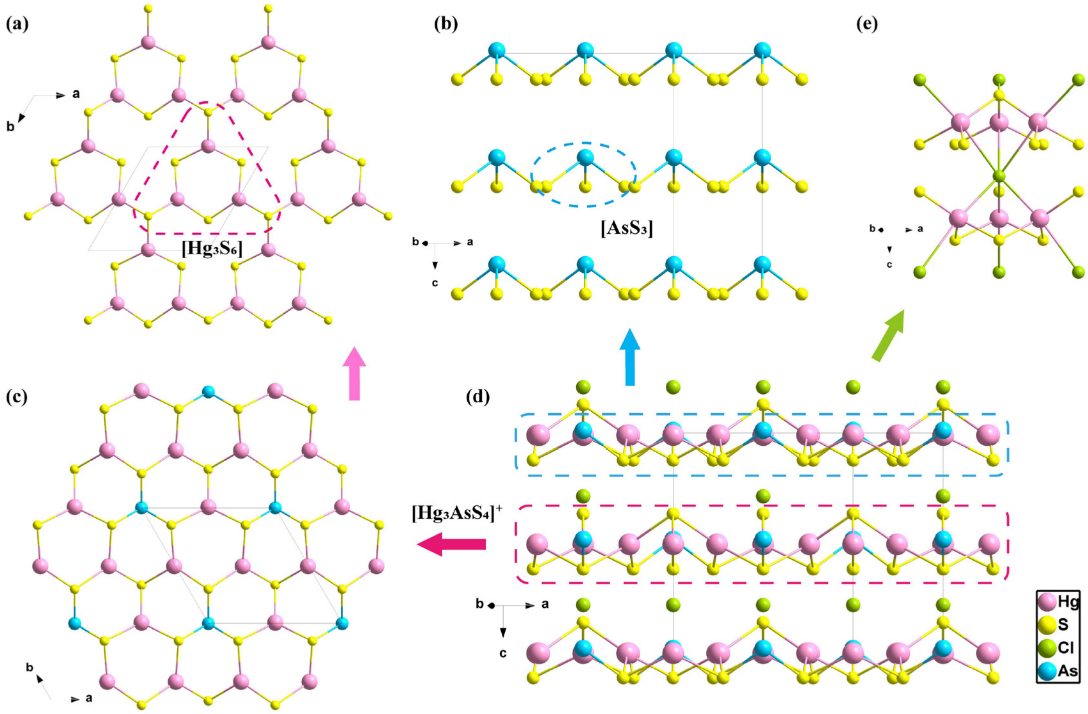

Fig. 1 (a) $[Hg_3S_6]$ unit and $[Hg_3S_6]$ groups, (b) $[AsS_3]$ unit and $[AsS_3]$ array, (c) infinite $[Hg_3AsS_4]^+$ layer, (d) crystal structure of HASC viewed in the (010) plane, and (e) connection of Cl atoms.

Optical properties

The UV-Vis-NIR transmittance spectrum of HASC and HASB, measured by utilizing polished crystal wafers (Fig. S1d and e†), exhibited a wide transmission range and displayed no obvious absorption peak ranges of 515–2500 nm and 510–2500 nm, respectively (Fig. 2a and b). The indirect band gap of HASC and HASB was estimated to be 2.408 eV and 2.431 eV, respectively, wider than that of some traditional IR NLO crystals, such as $AgGaSe_2$ (1.83 eV) and $ZnGeP_2$ (1.9 eV).[52,53] The IR transmission spectra of HASC and HASB were also recorded (Fig. 2a and b), which indicated that these two compounds possessed a broad transparency region of 2.5–13.7 μm and 2.5–14.2 μm, respectively. As a result, HASC and HASB was transparent over a wide range covering visible to IR region of 0.515–13.7 μm and 0.510–14.2 μm, respectively, significantly possessing expansive long-wave IR atmospheric window of 8–14 μm, which could be efficiently pumped by 1.064, 2.09 and 10.6 μm laser sources. Moreover, the Raman spectra of HASC and HASB were in agreement with the IR spectra. Additionally, as shown in the insets of Fig. 2c and d, several obvious absorption peaks were recorded in the region of 50–400 cm^{-1}. The Raman peaks below 300 cm^{-1} mainly originated from the vibrations of Hg–S bonds,[54] and the peaks above approximately 300 cm^{-1} belonged to the vibrations of the As–S bonds.[55] Furthermore, single crystal LDT measurements were carried out by a single pulse method for preliminarily evaluating the laser damage resistance of HASC and HASB. The results indicated the LDT of two crystals was 123 and 125 MW cm^{-2} @1064 nm, 1 Hz, 10 ns, respectively, which was much larger than that of AGS (30 MW cm^{-2} @1064 nm, 1 Hz, 10 ns) under the same experimental conditions.

The refractive index dispersion curves of HASC and HASB were also obtained and are presented in Fig. S4.† The calculated refractive indices as a function of wavelength were fitted by the least-squares method according to the Sellmeier equations: n_o^2 (or n_e^2) = $A + B\lambda^2/(\lambda^2 - C) - D\lambda^2$, where λ is the wavelength in μm and A–D are the parameters. The fitted Sellmeier equation for HASC was expressed as

$$n_o^2 = 1 + \frac{7.32438\lambda^2}{\lambda^2 - 0.08377} - 0.03762\lambda^2 \quad (1)$$

$$n_e^2 = 1 + \frac{4.93045\lambda^2}{\lambda^2 - 0.05646} - 0.01400\lambda^2 \quad (2)$$

And that for HASB was expressed as

$$n_o^2 = 1 + \frac{7.31309\lambda^2}{\lambda^2 - 0.08008} - 0.05196\lambda^2 \quad (3)$$

$$n_e^2 = 1 + \frac{5.07817\lambda^2}{\lambda^2 - 0.05733} - 0.02495\lambda^2 \quad (4)$$

The results indicated that they both had strong optical anisotropy with $n_o > n_e$. According to the fitted Sellmeier equations, the birefringence of HASC and HASB was also calculated to be 0.447 and 0.412 at 2050 nm, respectively, implying their outstanding PM capacity. The large optical anisotropy was created by asymmetric electron polarization along the c-axis in the $[Hg_3AsS_4]^+$ layer due to structural anisotropy, while Cl^-/Br^- contributed little to the birefringence due to the isotropic electron density distribution.[9]

The PL excitation and emission spectra of HASC and HASB were preliminarily recorded and are shown in Fig. 2e and f. Upon UV excitation at 248 nm, HASC and HASB all exhibited bright purple PL with a broad emission band (full-width at half maximum (FWHM) of ≈29.5 eV) at 390 nm at room temperature, which originated from the existence of point defects caused by sulfur vacancies in the structures.[56,57] These defects

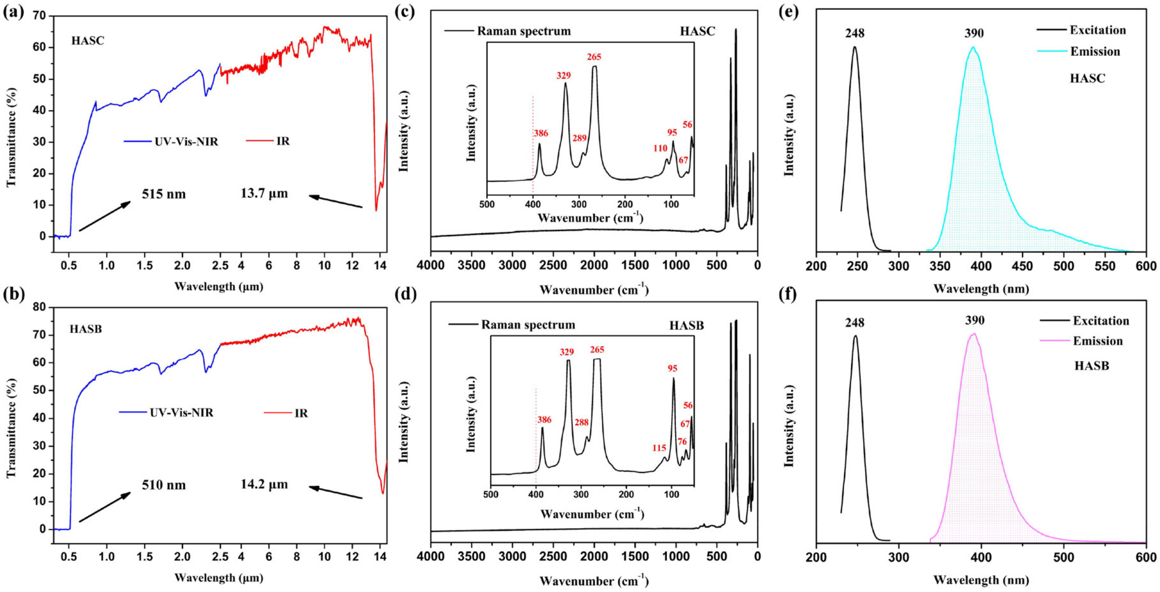

Fig. 2 UV-Vis-NIR and IR transmittance spectra for (a) HASC and (b) HASB, Raman spectrum for (c) HASC and (d) HASB, and PL excitation and emission spectra for (e) HASC and (f) HASB, respectively.

would be electron trapping centers, resulting in a high electron–hole pair recombination rate for luminescence. The PL decay curves of HASC and HASB displayed single-exponential decay with the fitted PL lifetime of 106.97 μs and 107.49 μs, respectively (Fig. S5a and b†). Generally, the appropriate Stokes shift would effectively avoid severe self-absorption and was conducive to luminescence. Fortunately, on account of exciton phonon coupling, the Stokes shifts of HASC and HASB were all of 142 nm, which was larger than that of some IR materials, such as $ACd_4Ga_5Te_{12}$ (A = K/Rb/Cs) (Stokes shifts of 65/72/72 nm), and some gallium sulfides (Stokes shifts of 72–125 nm), *etc.*,[58] indicating the capacity of HASC and HASB as luminescent materials. To further investigate the origin of PL, power-dependent PL intensity measurements were performed. The experimental results showed that the PL intensity gradually increased to the saturation value with the rise of power density (Fig. S5c and d†), confirming that PL of HASC and HASB both originated from defects. As PL from defects generally presented sublinear dependence on the power density with a saturation of limited defect sites under high excitation intensity.[59–63] Besides, the emission mechanism of HASC and HASB was further explored by measuring their PL spectra over the temperature range of 10–300 K (Fig. S5e and f†). A thermal enhancement of PL intensity was observed in both compounds as the temperature increased from 10 to 300 K, which was consistent with the characteristics of phonon-assisted luminescence in defect centers.[64,65] The increase in temperature allowed for a greater probability of the charge carriers to be captured at the deep defects, with more phonons becoming active and participating in the energy transfer process, and accordingly resulted in high multiples of enhanced PL intensity. On the whole, comparing to the PL of known chalcogenides, such as some gallium sulfides (PL at 440–500 nm),[58] $ZnIn_2S_4$ (PL at 775 nm), $Zn_3In_2S_6$ (PL at 681 nm), $CdGa_2S_4$ (PL at 577 nm),[66] $ACd_4Ga_5S_{12}$ (A = K, Rb, Cs) (PL at 574–595 nm),[67] $Ba_4MGa_4Se_{10}Cl_2$ (M = Zn, Cd, Mn, Cu/Ga) (PL at 697–880 nm),[68] $Ba_3AGa_5Se_{10}Cl_2$ (A = Cs, Rb, K) (PL at 711–731 nm),[69] *etc.*, it is unusual for HASC and HASB to observe luminescence output centered in the UV region in chalcogenides, which extended the emission region of chalcogenides and exhibited expansive potential optical applications of HASC and HASB.

Thermal analysis

The thermogravimetric (TG) analyses of HASC and HASB, as shown in Fig. S6a and b,† presented the stability up to about 305 °C and 330 °C, respectively, corresponding to endothermic peaks at 340 °C and 473 °C of the differential thermal analysis (DTA) curve for HASC, 380 °C and 460 °C of DTA curve for HASB, due to the decomposition of the compound through thermal disproportionation. The PXRD analyses at various temperatures confirmed that HASC and HASB had been decomposed into HgS at 380 °C and 400 °C (Fig. S6c and d†), respectively. The results further indicated bulk single crystals growth of HASC and HASB could be carried out by the chemical vapor transport technique instead of the mainstream crystal growth technique, the Bridgman method, because these two compounds were not melting-congruent.

NLO properties

The powder SHG measurements of HASC and HASB corresponding to different particle sizes, exhibited in Fig. 3a, were systematically carried out with AGS as references through the Kurtz and Perry method. Attributed to the introduction of Hg and As and the oriented arrangement of $[AsS_3]$ groups, HASC and HASB exhibited strong SHG responses, which were about 2.8 and 3.2 times that of AGS under 2050 nm laser irradiation (Fig. 3a), respectively, larger than that of some IR NLO chalcogenides under the same wavelength laser irradiation such as $LiGaS_2$ (~0.4 × AGS), $LiInS_2$ (0.54 × AGS),[70] $BaGa_2GeS_6$ (2.1 × AGS),[71,72] $AMg_3M_3S_8$ (A = Na, Ag; M = Al, Ga) (<1 × AGS),[73] $SrZnGeS_4$ (0.9 × AGS),[2] $Rb_2CdSi_4S_{10}$ (~0.6 × AGS),[74] $Eu_2P_2S_6$ (~0.9 × AGS),[75] *etc.* Furthermore, the second-order NLO susceptibilities of HASC and HASB were also investigated by first principal calculations. Since their space group belonged to class 6 mm, it had two independent nonvanishing NLO susceptibility tensors, d_{31} and d_{33}. The calculated NLO coefficients were $d_{31} = -18.3$ pm V^{-1} and $d_{33} = 17.6$ pm V^{-1} for HASC and $d_{31} = -23.3$ pm V^{-1} and $d_{33} = 18.5$ pm V^{-1} for HASB at a wavelength of 2050 nm (0.605 eV), respectively (Fig. 3b and c). It was noteworthy that d_{31} took practical significance in the SHG process of 6 mm class, and it could be seen that the calculated d_{31} was comparable to the results of powder SHG measurements.

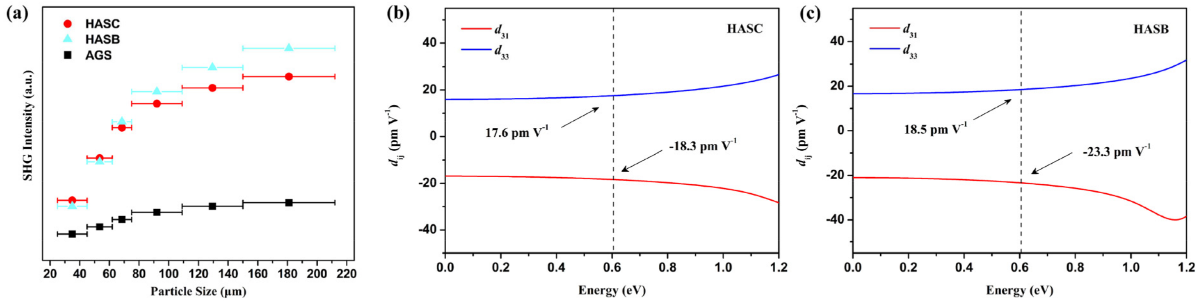

Fig. 3 (a) Particle size-dependent SHG intensity curves for HASC and HASB with reference of AGS under a 2050 nm laser. Calculated independent NLO coefficients for (b) HASC and (c) HASB.

According to the anionic group theory,[36] the SHG contribution mainly resulted from the dipole transition of the intra-atomic transitions in [HgS_3] and [AsS_3] groups. And the geometrical addition of the microscopic second-order susceptibility of these groups generated the macroscopic SHG effect of HASC and HASB. According to this calculated method (the specific calculation steps were expatiated in the ESI†),[76] the NLO coefficients were proportional to density of the groups (n/V), the structural criterion (C), and nonvanishing second-order susceptibility $\beta_{311}^{(2)}$ and $\beta_{333}^{(2)}$, respectively. The calculated results are listed in Table 2, where the C value of [AsS_3] groups for HASC and HASB were all 1, which means that the [AsS_3] groups were optimally arranged for a good SHG performance. Although the C value of [HgS_3] was inferior to that of [AsS_3] groups, respectively, a larger density of the groups (n/V) facilitated greater SHG contribution.

Besides, the dipole moments of [HgS_3] and [AsS_3] groups were also calculated to evaluate their contribution to macroscopical SHG effects, respectively.[77–79] The direction and magnitude of dipole moments of these groups are listed in Table 3. The x and y components of the six [HgS_3] groups in a unit cell were cancelled out and close to zero, while the z components of that added up to a total dipole moment of 13.956 D for HASC and 14.474 D for HASB without any cancellation, respectively. The x and y components of all the dipole moments for [AsS_3] groups were zero. The dipole moment of the two [AsS_3] groups was calculated to be 13.416 D for HASC and 13.576 D for HASB, respectively, which was derived from the z component of the polarization. The z components from all the [HgS_3] and [AsS_3] groups within one unit cell were summed up to a total dipole moment of 27.372 D for HASC and 28.050 D for HASB, respectively. Thus, it could be concluded that the constructively geometric superposition of dipole moments of [HgS_3] and [AsS_3] groups facilitated the appreciable SHG effect, where the polarization contributions of [HgS_3] and [AsS_3] groups were calculated to be 51.0% and 49.0% for HASC and 51.6% and 48.4% for HASB, respectively.

Table 2 Calculations of anionic group theory and SHG efficiencies for HASC and HASB

Group	Structural criterion C	Densities of the groups (n/V) ($Å^{-3}$)	(n/V) × C (×10^{-2} $Å^{-3}$)
Hg_3AsS_4Cl			
[HgS_3]	0.716	0.0138	0.99
[AsS_3]	1.000	0.0046	0.46
Hg_3AsS_4Br			
[HgS_3]	0.711	0.0134	0.95
[AsS_3]	1.000	0.0045	0.45

Table 3 Direction and magnitude of dipole moments of [HgS_3] and [AsS_3] groups

	Dipole moment (μ, unit: debye)		Total magnitude	
Polar unit in a unit cell	μ_x	μ_y	μ_z	μ_t
Hg_3AsS_4Cl				
[HgS_3](1) × 2	0	−1.282	−2.325	2.655
[HgS_3](2) × 2	−1.111	0.641	−2.328	2.658
[HgS_3](3) × 2	1.111	0.641	−2.325	2.655
[HgS_3] (total)	0	0	−13.956	13.956
[AsS_3] × 2	0	0	−6.708	6.708
[AsS_3] (total)	0	0	−13.416	13.416
Total	0	0	−27.372	27.372
Hg_3AsS_4Br				
[HgS_3](1) × 2	−1.088	0.624	−2.413	2.720
[HgS_3](2) × 2	1.088	0.633	−2.412	2.721
[HgS_3](3) × 2	0	−1.257	−2.412	2.720
[HgS_3] (total)	0	0	−14.474	14.474
[AsS_3] × 2	0	0	−6.788	6.788
[AsS_3] (total)	0	0	−13.576	13.576
Total	0	0	−28.050	28.050

Computational description

The band structures of HASC and HASB were calculated (as shown in Fig. S7†) and exhibited direct band gaps of 1.487 eV and 1.609 eV with the upper region of their valence band (VB) occurring at the M point and the bottom of their conduction band (CB) at the G point, respectively. The calculated value of the band gaps was smaller than the experimental value of 2.408 eV and 2.431 eV due to the underestimation of band gap by the density functional theory (DFT) method. Therefore, the scissor value of HASC and HASB can be set at 0.921 eV and 0.822 eV for the subsequent SHG calculations, respectively. Since the linear and NLO properties were mainly determined the forbidden band, formed by VB and CB, the total and partial densities of states (DOS and PDOS) of HASC and HASB were concentrated and are shown in Fig. S8.†[51] It can be observed that the upper part of VB was mainly composed of S 3p, Hg 6s, and Cl 3p/Br 4p orbitals, while the bottom part of CB was almost entirely dominated by S 3p, As 4p, and Hg 6s orbitals, demonstrating the covalent bonds of Hg–S and As–S corresponded to the linear and NLO properties such as the SHG effect. Furthermore, the electron density calculation was also carried out to infer and visualize SHG contribution of groups or atoms. The results were exhibited in Fig. S9,† further indicating that [HgS_3] and [AsS_3] groups were all playing important roles in the SHG process obviously. Besides, it is worth noting that Cl^-/Br^- anions also significantly contributed to the macro SHG effect, demonstrating that their second-order polarization could also be induced under optoelectronic field perturbation.

Conclusions

In summary, two Hg-based chalcogenides, Hg_3AsS_4Cl and Hg_3AsS_4Br, were synthesized by the chemical vapor transport technique, which revealed favorable NLO properties, encompassing strong SHG responses (2.8 and 3.2 × AGS), suitable band gaps (2.408 and 2.431 eV), large birefringence (0.447 and 0.412@2050 nm), broad transparency ranges (0.515–13.7 and 0.510–14.2 μm), and favorable LDT (123 and 125 MW cm^{-2}@1064 nm, 1 Hz, 10 ns). Besides, the PL excitation and emission spectra of these two compounds were preliminarily determined, respectively, showing that the broad emission band extended in the UV region and large Stokes shifts at room temperature. We believe that this work will promote HASC and HASB for broad optical and NLO applications and will have important implications for exploring IR NLO crystals on the basis of Hg-based chalcogenides.

Author contributions

N. Ye and F. Xu conceived and designed the calculations and experiments. F. Xu and J. Chen performed all the calculated and experimental works. C. Zheng and X. Xu provided discussion and suggestions and helped with the PL measurements and device maintenance. B. Li and G. Zhang performed the LDT measurements and some calculations. F. Xu wrote the manuscript. N. Ye and J. Chen revised the manuscript. All the authors discussed the results.

Conflicts of interest

There are no conflicts to declare.

Acknowledgements

This work was supported by the National Natural Science Foundation of China (52202011 and 22305174), the Natural Science Foundation of Fujian Province (2023J01158), the State Key Laboratory of Structural Chemistry (20230013), and Fujian University of Technology (GY-Z220191). The authors thank Dr Shaohua Yu and Chenliang Li in FJIRSM for helpful discussions.

References

1 A. Abudurusuli, J. Huang, P. Wang, Z. Yang, S. Pan and J. Li, $Li_4MgGe_2S_7$: The first alkali and alkaline-earth diamond-like infrared nonlinear optical material with exceptional large band gap, *Angew. Chem., Int. Ed.*, 2021, **60**, 24131–24136.

2 Q.-Q. Liu, X. Liu, L.-M. Wu and L. Chen, $SrZnGeS_4$: A dual-waveband nonlinear optical material with a transparency spanning UV/Vis and far-IR spectral regions, *Angew. Chem., Int. Ed.*, 2022, **61**, e202205587.

3 C.-L. Hu, Y.-X. Han, Z. Fang and J.-G. Mao, Zn_2BS_3Br: An infrared nonlinear optical material with significant dual-property enhancements designed through a template grafting strategy, *Chem. Mater.*, 2023, **35**, 2647–2654.

4 B.-W. Liu, X.-M. Jiang, B.-X. Li, H.-Y. Zeng and G.-C. Guo, Li $[LiCs_2Cl][Ga_3S_6]$: A nanoporous framework of GaS_4 tetrahedra with excellent nonlinear optical performance, *Angew. Chem., Int. Ed.*, 2020, **59**, 4856–4859.

5 D. Cyranoski, Materials science China's crystal cache, *Nature*, 2009, **457**, 953–955.

6 J. Chen, X. Jiang, Q. Wu, Z. Lin, M. Luo and N. Ye, Pnictides: An emerging class of infrared nonlinear optical material candidates, *J. Alloys Compd.*, 2022, **901**, 163384.

7 A. Abudurusuli, J. Li and S. Pan, A review on the recently developed promising infrared nonlinear optical materials, *Dalton Trans.*, 2021, **50**, 3155–3160.

8 G. C. Catella, L. R. Shiozawa, J. R. Hietanen, R. C. Eckardt, R. K. Route, R. S. Feigelson, D. G. Cooper and C. L. Marquardt, Mid-IR absorption in $AgGaSe_2$ optical parametric oscillator crystals, *Appl. Opt.*, 1993, **32**, 3948–3951.

9 J. Chen, C. Lin, X. Jiang, G. Yang, M. Luo, X. Zhao, B. Li, G. Peng, N. Ye, Z. Hu, J. Wang and Y. Wu, Honeycomb layered topology construction for exceptional long-wave infrared nonlinear optical crystals, *Mater. Horiz.*, 2023, **10**, 2876–2882.

10 K. Wu, B. Zhang, Z. Yang and S. Pan, New compressed chalcopyrite-like $Li_2BaM^{IV}Q_4$ (M^{IV} = Ge, Sn; Q = S, Se): promising infrared nonlinear optical materials, *J. Am. Chem. Soc.*, 2017, **139**, 14885–14888.

11 G. D. Boyd, E. Buehler and F. G. Storz, Linear and nonlinear optical properties of $ZnGeP_2$ and CdSe, *Appl. Phys. Lett.*, 2003, **18**, 301–304.

12 Q. Wu, C. Yang, X. Liu, J. Ma, F. Liang and Y. Du, Dimensionality reduction made high-performance mid-infrared nonlinear halide crystal, *Mater. Today Phys.*, 2021, **21**, 100569.

13 H. Chen, W.-B. Wei, H. Lin and X.-T. Wu, Transition-metal-based chalcogenides: A rich source of infrared nonlinear optical materials, *Coord. Chem. Rev.*, 2021, **448**, 214154.

14 M. Yan, Z.-D. Sun, W.-D. Yao, W.-F. Zhou, W.-L. Liu and S.-P. Guo, A highly distorted HgS_4 tetrahedron-induced moderate second-harmonic generation response of $EuHgGeS_4$, *Inorg. Chem. Front.*, 2020, **7**, 2451–2458.

15 Y. Guo, F. Liang, J. Yao, Z. Lin, W. Yin, Y. Wu and C. Chen, Nonbonding electrons driven strong SHG effect in Hg_2GeSe_4: experimental and theoretical investigations, *Inorg. Chem.*, 2018, **57**, 6795–6798.

16 C. Li, W. Yin, P. Gong, X. Li, M. Zhou, A. Mar, Z. Lin, J. Yao, Y. Wu and C. Chen, Trigonal planar $[HgSe_3]^{4-}$ unit: a new kind of basic functional group in IR nonlinear optical materials with large susceptibility and physicochemical stability, *J. Am. Chem. Soc.*, 2016, **138**, 6135–6138.

17 Y. Liu, F. Wei, S. N. Yeo, F. M. Lee, C. Kloc, Q. Yan, H. H. Hng, J. Ma and Q. Zhang, Synthesis, crystal structure, and optical properties of a three-dimensional quaternary Hg–In–S–Cl chalcohalide: $Hg_7InS_6Cl_5$, *Inorg. Chem.*, 2012, **51**, 4414–4416.

18 Y. Liu, P. D. Kanhere, Y. S. Hoo, K. Ye, Q. Yan, R. S. Rawat, Z. Chen, J. Ma and Q. Zhang, Cationic quaternary chalcohalide nanobelts: $Hg_4In_2Q_3Cl_8$ (Q = S, Se, Te), *RSC Adv.*, 2012, **2**, 6401–6403.

19 M.-Y. Li, Z. Ma, B. Li, X.-T. Wu, H. Lin and Q.-L. Zhu, $HgCuPS_4$: An exceptional infrared nonlinear optical

material with defect diamond-like structure, *Chem. Mater.*, 2020, **32**, 4331–4339.

20 C. Li, X. Meng, Z. Li and J. Yao, Hg-based chalcogenides: An intriguing class of infrared nonlinear optical materials, *Coord. Chem. Rev.*, 2022, **453**, 214328.

21 J. H. Liao, G. M. Marking, K. F. Hsu, Y. Matsushita, M. D. Ewbank, R. Borwick, P. Cunningham, M. J. Rosker and M. G. Kanatzidis, α- and β-$A_2Hg_3M_2S_8$ (A = K, Rb; M = Ge, Sn): Polar quaternary chalcogenides with strong non-linear optical response, *J. Am. Chem. Soc.*, 2003, **125**, 9484–9493.

22 Y. Chu, H. Wang, T. Abutukadi, Z. Li, M. Mutailipu, X. Su, Z. Yang, J. Li and S. Pan, $Zn_2HgP_2S_8$: A wide bandgap Hg-based infrared nonlinear optical material with large second-harmonic generation response, *Small*, 2023, **19**, 2305074.

23 Y. Chu, P. Wang, H. Zeng, S. Cheng, X. Su, Z. Yang, J. Li and S. Pan, $Hg_3P_2S_8$: A new promising infrared nonlinear optical material with a large second-harmonic generation and a high laser-induced damage threshold, *Chem. Mater.*, 2021, **33**, 6514–6521.

24 W. Xing, F. Liang, C. Tang, E. Uykur, Z. Lin, J. Yao, W. Yin and B. Kang, Highly distorted $[HgS_4]$ motif-driven structural symmetry degradation and strengthened second-harmonic generation response in the defect diamond-like chalcogenide $Hg_3P_2S_8$, *ACS Appl. Mater. Interfaces*, 2021, **13**, 37331–37338.

25 Y. Guo, F. Liang, Z. Li, W. Xing, Z.-S. Lin, J. Yao, A. Mar and Y. Wu, $AHgSnQ_4$ (A = Sr, Ba; Q = S, Se): A series of Hg-based infrared nonlinear-optical materials with strong second-harmonic-generation response and good phase matchability, *Inorg. Chem.*, 2019, **58**, 10390–10398.

26 K. Wu, Z. Yang and S. Pan, $Na_2Hg_3M_2S_8$ (M = Si, Ge, and Sn): New infrared nnlinear optical materials with strong second harmonic generation effects and high laser-damage thresholds, *Chem. Mater.*, 2016, **28**, 2795–2801.

27 W. Xing, C. Tang, P. Gong, J. Wu, Z. Lin, J. Yao, W. Yin and B. Kang, Investigation into structural variation from 3D to 1D and strong second harmonic generation of the $AHgPS_4$ (A^+ = Na^+, K^+, Rb^+, Cs^+) Family, *Inorg. Chem.*, 2021, **60**, 18370–18378.

28 Y. Zhang, H. Wu, Z. Hu, J. Wang, Y. Wu and H. Yu, Achieving a strong second harmonic generation response and a wide band gap in a Hg-based material, *Inorg. Chem. Front.*, 2022, **9**, 4075–4080.

29 W. Xing, C. Tang, N. Wang, C. Li, E. Uykur, J. Wu, Z. Lin, J. Yao, W. Yin and B. Kang, $AXHg_3P_2S_8$ (A = Rb, Cs; X = Cl, Br): New excellent infrared nonlinear optical materials with mixed-anion chalcohalide groups of trigonal planar $[HgS_2X]^{3-}$ and tetrahedral $[HgS_3X]^{5-}$, *Adv. Opt. Mater.*, 2021, **9**, 2100563.

30 Y. Xiao, M.-M. Chen, Y.-Y. Shen, P.-F. Liu, H. Lin and Y. Liu, $A_3Mn_2Sb_3S_8$ (A = K and Rb): a new type of multifunctional infrared nonlinear optical material based on unique three-dimensional open frameworks, *Inorg. Chem. Front.*, 2021, **8**, 2835–2843.

31 C. Liu, S.-H. Zhou, Y. Xiao, C. Zhang, H. Lin and Y. Liu, Aliovalent-cation-substitution-induced structure transformation: a new path toward high-performance IR nonlinear optical materials, *J. Mater. Chem. C*, 2021, **9**, 15407–15414.

32 E. H. Gamage, S. Kamali, J. K. Clark, Y. Lee, P. Yox, P. Shafer, A. A. Yaroslavtsev, L. Ke, M. Shatruk and K. Kovnir, As–Se pentagonal linkers to induce chirality and polarity in mixed-valent Fe–Se tetrahedral chains resulting in hidden magnetic ordering, *J. Am. Chem. Soc.*, 2022, **144**, 11283–11295.

33 A. K. Iyer, J. B. Cho, H. R. Byun, M. J. Waters, S. Hao, B. M. Oxley, V. Gopalan, C. Wolverton, J. M. Rondinelli, J. I. Jang and M. G. Kanatzidis, Structure tuning, strong second harmonic generation response, and high optical stability of the polar semiconductors $Na_{1-x}K_xAsQ_2$, *J. Am. Chem. Soc.*, 2021, **143**, 18204–18215.

34 A. Abudurusuli, K. Wu, A. Tudi, Z. Yang and S. Pan, $ABaSbQ_3$ (A = Li, Na; Q = S, Se): Diverse arrangement modes of isolated SbQ_3 ligands regulating the magnitudes of birefringences, *Chem. Commun.*, 2019, **55**, 5143–5146.

35 A. Cicirello, A. Swindle and J. Wang, Visualizing the alignment of lone pair electrons in $La_3AsS_5Br_2$ and $La_5As_2S_9Cl_3$ to form an acentric or centrosymmetric structure, *CrystEngComm*, 2023, **25**, 6354–6360.

36 C. Chen, Z. Lin and Z. Wang, The development of new borate-based UV nonlinear optical crystals, *Appl. Phys. B*, 2005, **80**, 1–25.

37 Y. Long, X. Dong, L. Huang, H. Zeng, Z. Lin, L. Zhou and G. Zou, $BaSb(H_2PO_2)_3Cl_2$: An excellent UV nonlinear optical hypophosphite exhibiting strong second-harmonic generation response, *Mater. Today Phys.*, 2022, **28**, 100876.

38 J. Huang, J. Cheng, B.-H. Lei, Z. Wei, S. Pan and Z. Yang, Synergism of multiple functional chromophores significantly enhancing the birefringence in layered non-centrosymmetric chalcohalides, *Inorg. Chem. Front.*, 2021, **8**, 1588–1598.

39 J. Beck, S. Hedderich and K. Köllisch, Hg_3AsE_4X (E = S, Se; X = Cl, Br, I), a family of isotypic compounds with an acentric, layered structure, *Inorg. Chem.*, 2000, **39**, 5847–5850.

40 G. Sheldrick, A short history of SHELX, *Acta Crystallogr., Sect. A: Found. Crystallogr.*, 2008, **64**, 112–122.

41 G. Sheldrick, SHELXT-integrated space-group and crystal-structure determination, *Acta Crystallogr., Sect. A: Found. Adv.*, 2015, **71**, 3–8.

42 A. Spek, Single-crystal structure validation with the program PLATON, *J. Appl. Crystallogr.*, 2003, **36**, 7–13.

43 S. K. Kurtz and T. T. Perry, A powder technique for the evaluation of nonlinear optical materials, *J. Appl. Phys.*, 1968, **39**, 3798–3813.

44 M. C. Payne, M. P. Teter, D. C. Allan, T. A. Arias and J. D. Joannopoulos, Iterative minimization techniques for ab Initio total-energy calculations: molecular dynamics and conjugate gradients, *Rev. Mod. Phys.*, 1992, **64**, 1045–1097.

45 S. J. Clark, M. D. Segall, C. J. Pickard, P. J. Hasnip, M. I. J. Probert, K. Refson and M. C. Payne, First principles methods using CASTEP, *Z. Kristallogr.*, 2005, **220**, 567.

46 J. P. Perdew, K. Burke and M. Ernzerhof, Generalized gradient approximation made simple, *Phys. Rev. Lett.*, 1996, **77**, 3865–3868.

47 L. Kleinman and D. M. Bylander, Efficacious form for model pseudopotentials, *Phys. Rev. Lett.*, 1982, **48**, 1425–1428.

48 H. J. Monkhorst and J. D. Pack, Special points for brillouin-zone integrations, *Phys. Rev. B: Solid State*, 1976, **13**, 5188–5192.

49 R. W. Godby, M. Schlüter and L. J. Sham, Self-energy operators and exchange-correlation potentials in semiconductors, *Phys. Rev. B: Condens. Matter Mater. Phys.*, 1988, **37**, 10159–10175.

50 E. Ghahramani, D. J. Moss and J. E. Sipe, Full-band-structure calculation of second-harmonic generation in odd-period strained $(Si)_n/(Ge)_n$ superlattices, *Phys. Rev. B: Condens. Matter Mater. Phys.*, 1991, **43**, 8990–9002.

51 M.-H. Lee, C.-H. Yang and J.-H. Jan, Band-resolved analysis of nonlinear optical properties of crystalline and molecular materials, *Phys. Rev. B: Condens. Matter Mater. Phys.*, 2004, **70**, 235110.

52 G. C. Catella and D. Burlage, Crystal growth and optical properties of $AgGaS_2$ and $AgGaSe_2$, *MRS Bull.*, 1998, **23**, 28–36.

53 X. Zhao, S. Zhu, B. Zhao, B. Chen, Z. He, R. Wang, H. Yang, Y. Sun and J. Cheng, Growth and characterization of $ZnGeP_2$ single crystals by the modified Bridgman method, *J. Cryst. Growth*, 2008, **311**, 190–193.

54 G. A. Marking, J. A. Hanko and M. G. Kanatzidis, New quaternary thiostannates and thiogermanates $A_2Hg_3M_2S_8$ (A = Cs, Rb; M = Sn, Ge) through molten A_2S_x. Reversible gass formation in $Cs_2Hg_3M_2S_8$, *Chem. Mater.*, 1998, **10**, 1191–1199.

55 A. Stronski, T. Kavetskyy, L. Revutska, I. Kaban, K. Shportko, J. Baran and M. Trzebiatowska, Stoichiometric deviations in bond distances in the mixed As_2S_3-As_2Se_3 system: Raman spectroscopy and EXAFS studies, *J. Non-Cryst. Solids*, 2019, **521**, 119533.

56 N. Chestnoy, T. D. Harris, R. Hull and L. E. Brus, Luminescence and photophysics of cadmium sulfide semiconductor clusters: the nature of the emitting electronic state, *J. Phys. Chem.*, 1986, **90**, 3393–3399.

57 P. S. Nair, T. Radhakrishnan, N. Revaprasadu, G. A. Kolawole and P. O'Brien, The synthesis of HgS nanoparticles in polystyrene matrix, *J. Mater. Chem.*, 2004, **14**, 581–584.

58 N. Zheng, X. Bu and P. Feng, Nonaqueous synthesis and selective crystallization of gallium sulfide clusters into three-dimensional photoluminescent superlattices, *J. Am. Chem. Soc.*, 2003, **125**, 1138–1139.

59 J. Luo, X. Wang, S. Li, J. Liu, Y. Guo, G. Niu, L. Yao, Y. Fu, L. Gao, Q. Dong, C. Zhao, M. Leng, F. Ma, W. Liang, L. Wang, S. Jin, J. Han, L. Zhang, J. Etheridge, J. Wang, Y. Yan, E. H. Sargent and J. Tang, Efficient and stable emission of warm-white light from lead-free halide double perovskites, *Nature*, 2018, **563**, 541–545.

60 M. Zhang, L. Zhao, J. Xie, Q. Zhang, X. Wang, N. Yaqoob, Z. Yin, P. Kaghazchi, S. Zhang, H. Li, C. Zhang, L. Wang, L. Zhang, W. Xu and J. Xing, Molecular engineering towards efficientwhite-light-emitting perovskite, *Nat. Commun.*, 2021, **12**, 4890.

61 Z. Yuan, C. Zhou, Y. Tian, Y. Shu, J. Messier, J. C. Wang, L. J. van de Burgt, K. Kountouriotis, Y. Xin, E. Holt, K. Schanze, R. Clark, T. Siegrist and B. Ma, One-dimensional organic lead halide perovskites with efficient bluish white-light emission, *Nat. Commun.*, 2017, **8**, 14051.

62 E. R. Dohner, A. Jaffe, L. R. Bradshaw and H. I. Karunadasa, Intrinsic white-light emission from layered hybrid perovskites, *J. Am. Chem. Soc.*, 2014, **136**, 13154–13157.

63 Q. Guan, H. Ye, T. Zhu, X. Zhang, S. You, J. Wu, Y. Zheng, X. Liu and J. Luo, Formamidine engineering the lattice distortion of chiral halide perovskites for efficient blue circularly polarized emission, *Adv. Opt. Mater.*, 2023, **11**, 2202726.

64 F. Libbi, P. M. M. C. de Melo, Z. Zanolli, M. J. Verstraete and N. Marzari, Phonon-assisted luminescence in defect centers from many-body perturbation theory, *Phys. Rev. Lett.*, 2022, **128**, 167401.

65 P. Dang, W. Wang, H. Lian, G. Li and J. Lin, How to obtain anti-thermal-quenching inorganic luminescent materials for light-emitting diode applications, *Adv. Opt. Mater.*, 2022, **10**, 2102287.

66 A. Machuga, R. Radu, V. Pintea, E. Arama, V. Zhitar and T. Shemyakova, X-Ray luminescence in $ZnIn_2S_4$, $CdGa_2S_4$ and $Zn_3In_2S_6$, 2007 International Semiconductor Conference, 2007.

67 H. Lin, L.-J. Zhou and L. Chen, Sulfides with strong nonlinear optical activity and thermochromism: $ACd_4Ga_5S_{12}$ (A = K, Rb, Cs), *Chem. Mater.*, 2012, **24**, 3406–3414.

68 Y.-Y. Li, P.-F. Liu, L. Hu, L. Chen, H. Lin, L.-J. Zhou and L.-M. Wu, Strong IR NLO material $Ba_4MGa_4Se_{10}Cl_2$: highly improved laser damage threshold via dual ion substitution synergy, *Adv. Opt. Mater.*, 2015, **3**, 957–966.

69 P. Yu, L.-J. Zhou and L. Chen, Noncentrosymmetric inorganic open-framework chalcohalides with strong middle IR SHG and red emission: $Ba_3AGa_5Se_{10}Cl_2$ (A = Cs, Rb, K), *J. Am. Chem. Soc.*, 2012, **134**, 2227–2235.

70 L. Isaenko, I. Vasilyeva, A. Merkulov, A. Yelisseyev and S. Lobanov, Growth of new nonlinear crystals $LiMX_2$ (M=Al, In, Ga; X=S, Se, Te) for the mid-IR optics, *J. Cryst. Growth*, 2005, **275**, 217–223.

71 X. Lin, Y. Guo and N. Ye, $BaGa_2GeX_6$(X=S, Se): New mid-IR nonlinear optical crystals with large band gaps, *J. Solid State Chem.*, 2012, **195**, 172–177.

72 V. V. Badikov, D. V. Badikov, V. B. Laptev, K. V. Mitin, G. S. Shevyrdyaeva, N. I. Shchebetova and V. Petrov, Crystal growth and characterization of new quaternary chalcogenide nonlinear crystals for the mid-IR: $BaGa_2GeS_6$ and $BaGa_2GeSe_6$, *Opt. Mater. Express*, 2016, **6**, 2933–2938.

73 L. Luo, L. Wang, J. Chen, J. Zhou, Z. Yang, S. Pan and J. Li, AIB3IIC3I-IIQ8VI: A new family for the design of infrared nonlinear optical materials by coupling octahedra and tetrahedra units, *J. Am. Chem. Soc.*, 2022, **144**, 21916–21925.

74 J. Zhou, Z. Fan, K. Zhang, Z. Yang, S. Pan and J. Li, $Rb_2CdSi_4S_{10}$: novel $[Si_4S_{10}]$ T2-supertetrahedra-contained infrared nonlinear optical material with large band gap, *Mater. Horiz.*, 2023, **10**, 619–624.

75 X. Huang, S.-H. Yang, X.-H. Li, W. Liu and S.-P. Guo, $Eu_2P_2S_6$: The first rare-earth chalcogenophosphate exhibiting large second-harmonic generation response and high laser-induced damage threshold, *Angew. Chem., Int. Ed.*, 2022, **61**, e202206791.

76 N. Ye, Q. Chen, B. Wu and C. Chen, Searching for new nonlinear optical materials on the basis of the anionic group theory, *J. Appl. Phys.*, 1998, **84**, 555–558.

77 P. A. Maggard, T. S. Nault, C. L. Stern and K. R. Poeppelmeier, Alignment of acentric $MoO_3F_3{}^{3-}$ anions in a polar material: $(Ag_3MoO_3F_3)(Ag_3MoO_4)Cl$, *J. Solid State Chem.*, 2003, **175**, 27–33.

78 K. M. Ok and P. S. Halasyamani, Mixed-metal tellurites: synthesis, structure, and characterization of $Na_{1.4}Nb_3Te_{4.9}O_{18}$ and $NaNb_3Te_4O_{16}$, *Inorg. Chem.*, 2005, **44**, 3919–3925.

79 H. K. Izumi, J. E. Kirsch, C. L. Stern and K. R. Poeppelmeier, Examining the out-of-center distortion in the $[NbOF_5]^{2-}$ anion, *Inorg. Chem.*, 2005, **44**, 884–895.